Biochimica et Biophysica Acta 1850 (2015) 1286–1296

Contents lists available at ScienceDirect

Biochimica et Biophysica Acta

journal homepage: www.elsevier.com/locate/bbagen

Rescue of the temperature-sensitive, autosomal-recessive mutation R298S in the sodium-bicarbonate cotransporter NBCe1-A characterized by a weakened dimer and abnormal aggregation

Harindarpal S. Gill *, Kun-Young Choi, Lakshmi Kammili, Anastas Popratiloff

Department of Medicine, The George Washington University; Division of Renal & Hypertension, The GW Medical Faculty Associates, 2300 I (eye) Street NW, Ross Hall Room 436B, Washington D.C. 20052, United States

ARTICLE INFO

Article history:
Received 29 August 2014
Received in revised form 15 February 2015
Accepted 23 February 2015
Available online 3 March 2015

Keywords:
Protein aggregation
Composition-gradient light scattering
X-ray crystallography
Confocal microscopy

ABSTRACT

Background: Band keratopathy, an ocular disease that is characterized by hypercalcemia and opaque bands across the cornea, has been associated with kidney disease. Type-II renal tubular acidosis (RTA), a condition in which the kidneys fail to recover bicarbonate (HCO_3^-) in the proximal tubule of the nephron, results in HCO_3^- wastage in the urine and low blood pH. The development of these diseases is associated with autosomal-recessive mutations in the Na^+-coupled HCO_3^- cotransporter NBCe1-A located at the basolateral membranes of either cell type.
Methods: We provide insight into the devastating R298S mutation found in type-II RTA-afflicted individuals using confocal-microscopy imaging of fluorescently-tagged NBCe1-A and NBCe1-A-R298S molecules expressed in human corneal endothelial and proximal tubule cells and from in-depth biophysical studies of their cytoplasmic N-terminal domains (Nt and Nt-R298S), including Nt crystal structure, melting-temperature, and homodimer dissociation constant (K_D) analyses.
Results: We illuminate and rescue trafficking defects of the R298S mutation of NBCe1-A. The K_D for Nt monomer–dimer equilibrium is established. The K_D for Nt-R298S is significantly higher, but immeasurable due to environmental factors (pH, temperature, concentration) that result in dimer instability leading to precipitation. The crystal structure of Nt-dimer shows that R298 is part of a putative substrate conduit and resides near the dimer interface held together by hydrogen-bond networks.
Conclusions: The R298S is a temperature-sensitive mutation in Nt that results in instability of the colloidal system leading to abnormal aggregation.
General significance: Our findings provide new perspectives to the aberrant mechanism of certain ocular pathologies and type-II RTA associated with the R298S mutation.

1. Introduction

Bicarbonate (HCO_3^-) transport is essential for acid-base homeostasis in the body. The $NaHCO_3$ cotransporter NBCe1 is an integral membrane protein that regulates the pH of intracellular and interstitial fluids through regulation of Na^+ and HCO_3^- transport across cell membranes in many tissues including kidney, eye, heart, brain, among others [1–4]. NBCe1-A is abundant in the basolateral membrane of the renal proximal tubule and is also found in the thick ascending loop of Henle at trace levels [5], where it mediates a crucial step in the transepithelial movement of HCO_3^- ions and maintains blood pH. Impaired bicarbonate reabsorption, diagnosed in patients as proximal renal tubular acidosis (pRTA), or type-II RTA, is characterized by hyperchloremic metabolic acidosis (or a nonionic gap) with variable hypokalemia [6]. Typically, affected patients have a low blood pH of ~7.08 with HCO_3^- levels of ~5–6 mEq/L [7,8], while normal levels are considered to be 7.35–7.45 and 25–29 mEq/L, respectively [9].

NBCe1 has been implicated in a number of diseases affecting various organ systems. Prior studies have demonstrated that NBCe1 variants also play a key role in maintaining ocular pressure and corneal clarity. NBCe1 defects in ocular tissue have been associated with glaucoma, band keratopathy (calcium deposition along the stroma), and cataracts [10,11]. Additionally, NBCe1 variants participate in pH regulation of extracellular brain space, and are thought to modulate neuronal excitability in astrocytes by regulating local pH [12,13]. Inhibition of normal NBCe1 function is sometimes associated with mental retardation, accompanied by type-II RTA [11,13–15] and/or familial hemiplegic migraine [11,13]. It has also been suggested that NBCe1 is involved in enamel and tooth development [16,17]. Patients with loss of NBCe1-A activity exhibit abnormal "chalk-white" and brittle dentition [17].

Studies of patients affected by abnormal NBCe1 activity have led to the identification of a consistent, naturally occurring mutation, R298S, in the cytoplasmic N-terminal domain (Nt) of NBCe1. This mutation is

* Corresponding Author: Tel.: +1 202-994-4587; fax: +1 202-994-4538.
E-mail address: hgill@gwu.edu (H.S. Gill).

http://dx.doi.org/10.1016/j.bbagen.2015.02.014
0304-4165/

separate among others found in the transmembrane domain (TMD) [7,10]. The effect of the R298S mutation remains controversial in the literature. The studies first describing this mutation noted an uncharacterized functional defect in experiments using the human endothelial cell line ECV304 as a model system [7,18]. ECV304 cells were eventually reported to be an epithelial bladder cancer cell line and unsuitable for a model system [7,18]. Later studies using *Xenopus* oocytes also revealed effects of diminished trafficking (41% surface expression compared to wild type) [8]. In conflict, the laboratory of Romero showed that NBCe1-A-R298S expressed in *Xenopus* oocytes affects only NBCe1 function, and not NBCe1 protein processing or trafficking, by citing surface expression comparable to that of wild-type NBCe1-A and speculating on defective HCO_3^- permeation through the Nt [19]. Their suggested permeation defect, inferred from a homology model, was apparently demonstrated through experiments in which an engineered R298E mutation phenotype was rescued with an E91R mutation [19]. These experiments did confirm a complementary interaction between the two residues that was previously suggested in the crystal structure of NtAE1, the cytoplasmic N-terminal domain of AE1 also known as Band 3 [20]. This study, however, did not investigate nor consider the biochemical or physiological effects produced by the R298S mutation. Lastly, conflicting studies in yet another species, canine MDCK cells, with those initial *Xenopus* oocytes studies also have shown that the R298S mutation only affects function and not trafficking [21]; however these studies did not consider environmental variables known to influence animal cells [22] and later studies showed that MDCK cells are heterogeneous [23].

In our previous studies on the Nt of NBCe1 (residues 1 to 362), we set precedence for a monomer–dimer equilibrium and a multimodal system associated with conformational changes influenced by both pH and protein concentration [24,25]. Self-association of the Nt of NBCe1 is similar to that displayed by NtAE1, the later of which drives both dimer and the predominate tetramer formation of full-length AE1 [26,27]. Though, no K_D has been determined for the monomer–dimer equilibrium of NtAE1. In our earlier attempt to calculate the K_D of the Nt of NBCe1 with surface-plasmon-resonance analysis, we were hampered by this technique's inability to distinguish more than two protein states in equilibrium or determine their relative ratios that are a function of protein concentration.

In this report, for the first time, we monitored trafficking of NBCe1-A-R298S in HK-2 cells, a well-characterized immortalized line derived from human epithelial renal proximal tubule (PT) that has the same characteristics as normal adult proximal tubular cells [28], and in human corneal endothelial (HCE) cells. To study the effects of the R298S mutation, we investigated the molecular mechanisms behind self-association of the Nt of NBCe1. We report the crystal structure of the Nt, which is the only member of the sodium-coupled bicarbonate transporter (NCBT) family to be solved, illustrating for the first time extended-solvent accessible loops and substrate conduits that traverse the Nts of NBCe1 and AE1. In addition, the K_D of Nt self-association in solution has now been determined using composition-gradient multi-angle light scattering techniques. Finally, we demonstrated that the R298S mutation produces an unstable monomer–dimer equilibrium that leads to non-specific aggregation and time-dependent precipitation. The efficacy of our biophysical analyses was tested in live cells.

2. Material and methods

2.1. Mammalian and bacterial expression constructs

The green fluorescent protein (GFP) was translationally fused with full-length NBCe1-A using the pcDNA3.1/NT-GFP-TOPO mammalian expression vector (Life Technologies Corporation, Carlsbad, CA). PCR amplification for the TOPO-reaction was performed with Platinum Taq DNA Polymerase High Fidelity™ (Life Technologies, Cat No. 11304011). The NBCe1-A-R298S mutant in the same mammalian vector was generated by site-directed mutagenesis using the full-length NBCe1-A template above and Turbo-Pfu™ polymerase (Agilent Technologies, Santa Clara CA) for amplification according the manufacturer's protocol. The bacterial expression construct for Nt-NBCe1-A (Nt, residues 1-365), whose cDNA sequence was inserted into the pET15B vector (Life Technologies), is described in Gill & Boron, 2006. Here, a non-cleavable glycine codon followed by a six-histidine codon stretch preceded the first methionine of the Nt. The Nt-NBCe1-A-R298S mutant (Nt-R298S) using the same bacterial construct was prepared by site directed mutagenesis similar to the procedures cited above. The GFP-NBCe1-A, GFP-NBCe1-A-R298S, Nt, and Nt-R298S constructs were sequenced (Keck Facility, Yale University, CT).

2.2. Cell culture and electroporation

Cultured human kidney, proximal tubule cells (HK-2, ATCC® No. CRL2190) were grown at 37 °C in an atmosphere of 5% CO_2 and 95% air and cultured in 10 ml of keratinocyte serum-free media supplemented with 0.05 mg/ml bovine pituitary extract (BPE) and 5 ng/ml human recombinant epidermal growth factor (EGF 1-53) supplied in the kit (Life Technologies, Cat No. 17005042). The HCE cells were a gift from Dr. Jospeh A. Bonanno (Indiana University). In-depth characterization of HK-2 cells can be found in Ryan et al. [28] and HCE cells can be found in Schmedt et al. [29]. HCE cells were similarly grown in 10 ml of Optimem I (Life Technologies Cat No. 51985), 0.08 mg/ml chondroitin sulfate (Sigma, Cat No. C9819), 200 mg/L $CaCl_2$, 8% (v/v) fetal bovine serum (Hyclone, Cat No. SH30070.03), 0.1 mg/ml BPE (Biomedical Technologies, Cat No. BT-215), 0.5% (v/v) gentamycin (Life Technologies, Cat No. 15710), 5 ng/ml EGF (Millipore, Cat No. 01-101), and 1% antibiotic/antimycotic (Life Technologies, Cat No. 15240-062). Both type of cells were grown on 100 × 20 mm polystyrene tissue-culture dishes. Fresh media was added to cells every 2–3 days. At 80–90% confluency, adherent cells were trypsinized for 5 min with 3 ml 0.05% (w/v) trypsin-0.53 mM EDTA solution (Life Technologies, Cat No. 25300-054); the trypsin was inactivated with 8 ml media. The cells were then harvested by centrifuging 8 min at 125 ×*g* at 4 °C. For electroporation, the cell pellet was washed in half its original volume of ice-cold RPMI 1640 buffer (without phenol red and glutamine) (Biosource, Rockville, MD, Cat No. P149-500) and then harvested again. Cells were then resuspended in RPMI 1640 buffer at 5×10^6 cells per 775 μl and mixed with 50 μg DNA for total volume of 800 μl. Cells were then transferred into cuvettes and electroporated using a GenePulser Xcell™ (Biorad, Hercules CA) at maximum high capacitance with settings of 250 V and a high capacitance of 1000 μF. The cells were placed on ice for 10 min and diluted 3 to 4-fold with media. Transfections were repeated a minimum of three times. Transfection efficiencies were about 10%. These transformed cell lines were used as model expression systems.

2.3. Immunofluorescent staining and confocal microscopy

HK-2 and HCE cells electroporated with GFP-NBCe1-A or GFP-NBCe1-A-R298S were seeded at a density of 5×10^5 cells per 35-mm glass-bottom petri-dishes gel-coated with poly-D-lysine (BD Biocoat, Cat No. 354077) in 2 ml respective media. For protein-trafficking studies, after two days growth, 2 h prior to examination, the cells were incubated with a 2:1000 dilution of wheat germ agglutinin conjugated to Alexa Fluor 633™ (WGA-AF633, Life Technologies, Cat No. W21404) to outline the plasma membrane and similarly with the dye HOECHST 33342 (Invitrogen, Cat No. H3570) to label the nucleus; the markers were directly diluted into the cell culture. Confocal imaging was used to identify the labeled-membranes and to examine the intracellular trafficking of GFP-NBCe1-A and GFP-NBCe1-A-R298S. Colocalization of GFP with WGA-AF633 indicated plasma membrane association of GFP-tagged NBCe1-A.

For cell-polarization studies, cells grown on 35-mm dishes coated with poly-D-lysine were washed twice, 5 min each, with 1× phosphate buffered saline (PBS, Life Technologies, Cat No. AM9624) at pH 7.4 and

then fixed with 4% paraformaldehyde in 0.1 M PBS (Electron Microscopy Sciences, Cat No. 15735-85) at room temperature for 15 min. Cells were similarly washed and then permeabilized with 0.2% Triton X-100 (Fisher Scientific) in PBS for 5 min. Thereafter, cells again were washed twice for 5 min and blocked with 1.5% goat serum diluted in PBS (Santa Cruz Biotechnology Inc., Cat No. SC-2018) for 30 min at room temperature. After removing the blocking buffer, cells were washed twice and then incubated overnight with rabbit polyclonal primary antibody against Na^+/K^+-ATPase α-1 (EMD Millipore, Temecula, CA, Cat No. 06-520) using a 1:50 dilution in PBS at 4 °C temperature. After removing the primary antibody, cells were washed three times with PBS and incubated with goat anti-Rabbit IgG (H+L) secondary antibody conjugated to Alexa Fluor 555 (Life Technologies, Cat No. A21429) at 1:1000 dilution in PBS for 45 min at room temperature. Lastly, cells were washed three times with PBS and subsequently stored in PBS. Confocal imaging was used to identify basolateral-membranes by the localization of Na^+/K^+-ATPase. A similar procedure to demonstrate the efficacy of HK-2 cell polarization capability was implemented in Wang et al. [30], whose findings are consistent with the results shown in Supplementary Data.

Images were captured on a Carl Zeiss spinning disk confocal microscope based on Axio Observer Z1 inverted microscope. The spinning disk system was equipped with a 100×/1.46 objective lens (alpha Plan-Apochromat, Carl Zeiss). Images were acquired with Evolve Delta EM-CCD camera at 512 × 512 pixels. With this setup the pixel measured 0.133 μm. HOECHST was excited with a 405-diode laser line and the emission was captured with band pass 525/50. GFP was excited with a 488 diode, while the emission was captured with 535/30-emission filter. Finally, the WGA-AF633 was excited with a 633 diode and the emission captured with 690/50-band pass filter. Sequential images were acquired at 16 bit/pixel allowing normalizing for top and bottom of the intensities without truncation of the image data. Thus with the selected exposure times most of the signal was registered within the lower 20% of the available dynamic range, and for visualization the images were normalized using minimum and maximum values. Although the camera used was a low noise, the gain was set not to exceed 500 eV in order to minimize the white noise. Z-stacks were captured through the volume of GFP positive cells using software determined optimal z-step.

Image acquisition was done using the Zen Blue software (Carl Zeiss), while most of the analyses and visualization was done using Zen Black software (Carl Zeiss) or Imaris software (Bitplane Scientific Solutions, UK).

2.4. Purification with out-of-equilibrium molecular-mass measurements of Nt and Nt-R298S

The purification of Nt and Nt-R298S followed the protocol as previously described [25,31]. Briefly, after lysis and streptomycin precipitations of an 11 wet-gram *Escherichia coli* pellet, the soluble fraction was applied to a nickel-column (1-ml bed volume, Superflow™, Qiagen) and washed with 10-ml of 20 mM Imidazole pH 7.0 in 20 mM Tris pH 7.0, 150 mM NaCl, and 0.2% ß-mercaptoethanol. A step elution from the nickel column using 4-ml of 300 mM Imidazole pH 7.0 in 20 mM Tris pH 7.0, 150 mM NaCl, and 0.2% ß-mercaptoethanol buffer was then applied without concentration over a Superdex-200 (26/60) column (GE Healthcare) equilibrated with 50 mM Tris 7.3, 150 mM NaCl, and 1 mM TCEP buffer. Here, in the final step, weighted-averaged molecular masses (M_W) of each peak and extinction coefficients were measured by flowing the eluent from the size-exclusion column into a serially connected (online) multiangle light scattering (MALS) detector (MiniDAWN TREOS, Wyatt Technologies Corporation, Santa Barbara, CA) and then to a refractive-index detector (Optilab Trex, Wyatt Technologies Corporation) before fractionation. Protein concentration was determined by measuring the absorbance at 280 nm implemented in the Beer-Lambert Law, using the measured extinction coefficient of ~730 mL/(g ∗ cm) for the full-length Nt and Nt-R298S, and confirmed by Bradford assays. Data was processed using the ASTRA VI software package (Wyatt Technologies Corporation).

2.5. Dynamic light scattering (DLS) and in-equilibrium molecular-mass measurements

From the Superdex-200 (26/60) column, the peak fraction also was analyzed in batch mode (2 or 10 μl) using a dynamic-light scattering detector (DynaPro Nanostar, Wyatt Technology Corporation) that is supplemented with a single static detector. Here, the peak fraction already contained ~0.4–0.5 mg/ml protein. Concentration was avoided to minimize dimer self-associations for hydrodynamic radius (R_H) measurements. Samples were not filtered to avoid disturbing the equilibrium. Particularly for melting temperature experiments, the 2 μl sample was placed in a quartz cuvette and covered with ~2 μl mineral oil to avoid evaporation. Prior to taking measurements, the samples were allowed to equilibrate in the cuvette as judge by minimal fluctuations in the averaged scattered light and properly formed auto-correlation functions indicating initial low masses. Both R_H and melting-temperature (T_m) measurements were then performed. The initial temperature was 25 °C and ramped to 70 °C at a rate of 1 °C/min. Data were captured approximately every 0.5 min. Each measurement is composed of 5 acquisitions for 5 s each. Data were analyzed with the DYNAMICS software version 7.

2.6. Composition-gradient multiangle light scattering (CG-MALS)

CG-MALS experiments [32–34] were performed for the Nt. Composition gradients were created using the Calypso II hardware (Wyatt Technology Corporation) and delivered to an online UV/Vis concentration detector (Waters Corporation, Milford, Massachusetts) and a DAWN HELEOS II (Wyatt Technology Corporation) MALS detector. An embedded DLS detector within the HELEOS enabled simultaneous measurement of R_H and weight-average molar mass (M_W). Stock solutions of each protein were filtered to 0.02 μm, breaking any possible large clusters, using a syringe-tip filter (Whatman) prior to loading. For each composition in the automated method, nine concentrations of protein were prepared and passed through the MALS and UV detectors. After each injection, the flow was stopped for 60 s to allow the solution to come to equilibrium in the MALS flow cell. Data collection and analysis of equilibrium association constants were performed using the CALYPSO software version 2.1.3. Light scattering data from three composition gradients spanning concentrations 4.7 μg/ml to 1.2 mg/ml were concatenated and analyzed using the CALYPSO software to determine the K_D or the self-association affinity and stoichiometry for Nt.

2.7. X-ray crystallography: partial backbone structure of Nt

As reported in a preliminary communication [35], data were collected on Nt crystals in space group $P3_1$ with unit cell dimensions 51.7 Å × 51.7 Å × 200.4 Å, 90° 90° 120°. A Matthews coefficient [36,37] of 1.9 $Å^3$/Da was calculated on the basis of one Nt dimer in the asymmetric unit. Crystal Packing of Nt was determined using molecular replacement techniques by the program PHASER [38] using one NtAE1 dimer (PDBid:1HYN) as a probe with nonconserved residues truncated to alanine, as justified by the sequence similarity.

Herein, the probe was then truncated to one subunit. A cross-validated test set was chosen by picking reflections equally distributed over the resolution range. This test set consists of 10% of total reflections. Initial positional and B-factor refinement were implemented, with 2-fold non-crystallographic (NCS) constraints imposed on the subunit. Model building was then implemented, using the program ONO [39]. The model was partially built into 2-fold NCS-averaged maps, only where the electronic density was clearly observed. Maps were calculated by the SigmaA-weighted protocols in XPLOR (version 3.843),

with a resolution range of 44.7–3.5 Å resolution. Map averaging was calculated by the program suite RAVE [40]. The model was refined to 3.5-Å resolution using subsequent iteration cycles of rigid-body and position refinement, applying a strict 2-fold NCS constraint in XPLOR and in CNS (version 1.2). The Nt dimer was then generated from the subunit and positionally refined without constraints. At this point, due to the low data-to-parameter ratio, only one iteration of positional and B-factor refinements was performed for a final R-factor of 32.7% and R-free of 36%. The electron density of the residues 1 to 62 was absent, and those of non-conserved side-chains were not always interpretable and were not built—especially in the loop regions. Final model statistics are shown in Table 1 of Supplementary Data.

2.8. In silico analysis

The 3.5-Å resolution model of the Nt and the 2.6-Å resolution crystal structure of NtAE1 using the P and Q-chains of PDBid:1HYN [20] were superimposed. Root-Mean Square Deviation (RMSD) was calculated by secondary-structure matching (SSM) procedures in the program COOT [41]. Because of the high similarity of the tertiary fold of the backbones, the higher resolution core structure of NtAE1 was used to illuminate putative entrances and tunnels within the Nts. The program PYMOL was used to make surface representations and illuminate putative entrances. The program CAVER was implemented to objectively compute accessible routes within the Nt core, using a probe of radius 1.4 Å that approximates a water molecule.

3. Results

3.1. Trafficking defects Of NBCe1-A-R298S in human PT and HCE cells

As shown in Figs. 1 & 2, to examine the surface expression of NBCe1-A in human cells, GFP-tagged NBCe1-A and NBCe1-A-R298S were transiently expressed in immortalized HK-2 and HCE cells that were polarized on coated coverslips. Protein movement in live cells was monitored in real-time by green-fluorescent signals using a confocal microscope equipped with a 5% CO_2 stage-incubator. Small vesicles resembling post-Golgi cargo vesicles could be observed to traffick and fuse with the plasma membrane. Presumed early or late endosomes were generally identifiable as larger vesicles internalized from post-plasma membranes, which were identified by red-fluorescence from the WGA-AF633 stain, in contrast to the smaller cargo vesicles.

HK-2 cells transfected with wildtype GFP-NBCe1-A exhibited both green and red fluorescence at the basolateral plasma membrane. HK-2 cells transfected with GFP-NBCe1-A-R298S showed little-to-no green fluorescent signal at the plasma membrane but intracellular retention in cargo vesicles that were unable to fuse with the plasma membrane compared to the cells transfected with GFP-NBCe1-A. Fig. 1A exemplifies a transfected cell with plasmid encoding GFP-NBCe1-A (confluent among other non-transfected cells) that shows an intense surface signal of green fluorescence. Dual emission from the red surface marker and the green fluorescence appear yellowish-orange in the lower right panel, confirming that GFP-NBCe1-A in the transfected cell localized at the plasma membrane. Green fluorescence also localized inside the cells in vesicular cellular organelles supporting effective transport of GFP-NBCe1-A from Golgi to the membrane. In all successfully transfected cells ($n = 30$), GFP-NBCe1-A localized at the plasma membrane. Our findings are consistent with studies using other cell lines transfected with the same expression construct that GFP fused at the amino terminus does not effect affect trafficking [8,13,19,42,43]. On the other hand, Fig. 1B exemplifies three transfected cells with plasmid encoding GFP-NBCe1-A-R298S—two exhibiting no plasma membrane expression and the other with only a faint signal of green fluorescence at the plasma membrane. In addition, all three cells in the figure show large aggregations of green fluorescence retained intracellularly in vesicles. In all successfully transfected cells ($n = 30$), green fluorescence of 90% of observed cells expressing GFP-NBCe1-A-R298S was completely retained in vesicles in the cytoplasm, while 10% GFP-NBCe1-A-R298S showed a very limited amount of surface localization on the plasma membrane compared to wildtype. Of those vesicles that managed to traffick to the plasma membrane in post-Golgi transport vesicles, a small percentage (~1%) failed to fuse.

HCE cells transfected with wildtype GFP-NBCe1-A also exhibited both green and red fluorescence at the basolateral plasma membrane. HCE cells transfected with GFP-NBCe1-A-R298S demonstrated string-like aggregation localized near the plasma membrane in contrast to HCE cells transfected with GFP-NBCe1-A. Both panels of Fig 2 are similar to the experiments above in that red fluorescence was observed at the plasma membrane and intracellularly from membranes of post-Golgi

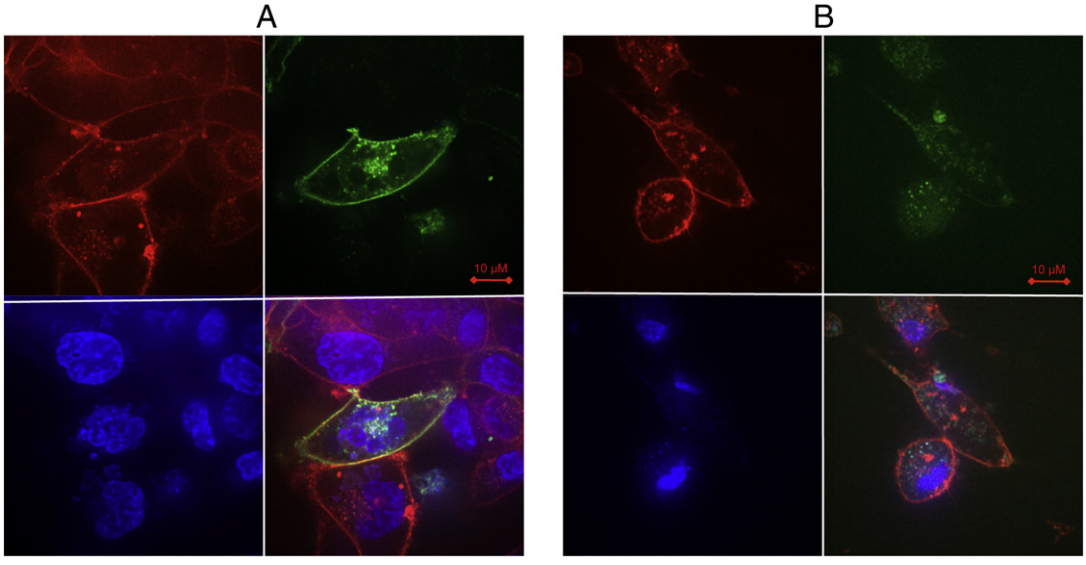

Fig. 1. Trafficking defects and aggregation of NBCe1-A-R298S in HK-2 cells. The trafficking movement of fluorescent signal from GFP-labeled **A.** Wildtype NBCe1-A and **B.** NBCe1-A-R298S were each monitored in real-time using live cells. Upper left panels mark the plasma membrane with (red) WGA-AF633; upper right panels correspond to the (green) fluorescence from GFP fused to NBCe1-A or NBCe1-A-R298S mutant; lower left panels correspond to the (blue) fluorescence from the dye HOECHST 33342, which marks the nucleus; lower right panels are dual excitations of the red and green fluorescence, which when overlapped appears yellow or orange.

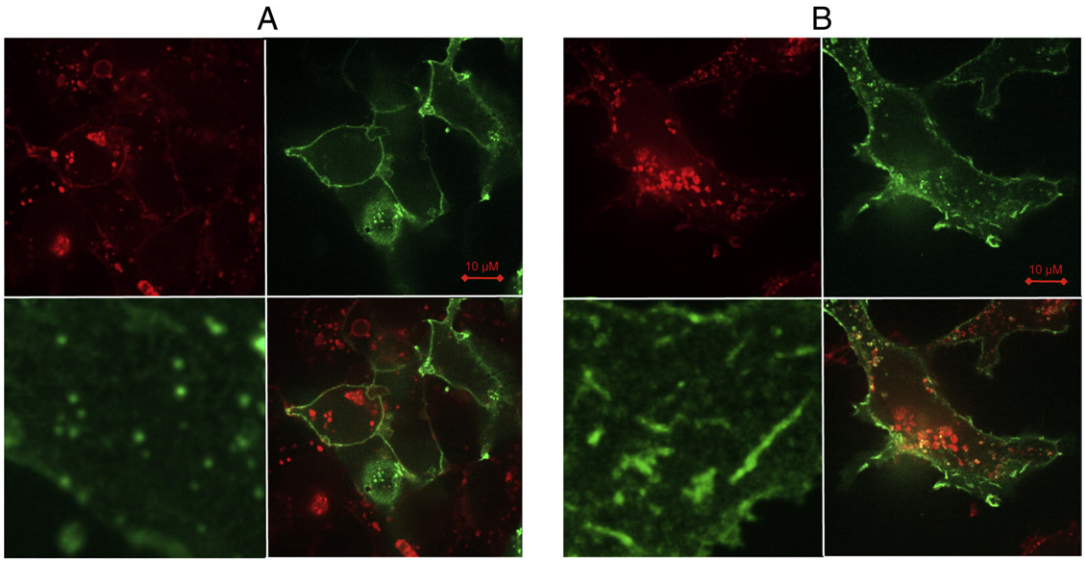

Fig. 2. Trafficking defects and aggregation of NBCe1-A-R298S in HCE cells. The trafficking movement of fluorescent signal from GFP-labeled **A.** Wildtype NBCe1-A and **B.** NBCe1-A-R298S were each monitored in real-time using live cells. Upper left panels mark the plasma membrane with (red) WGA-AF633; upper right panels correspond to the (green) fluorescence from GFP fused to NBCe1-A or NBCe1-A-R298S mutant; lower left panels are images of the same cells in 3D; lower right panels are dual excitations of the red and green fluorescence, which when overlapped appear yellow or orange.

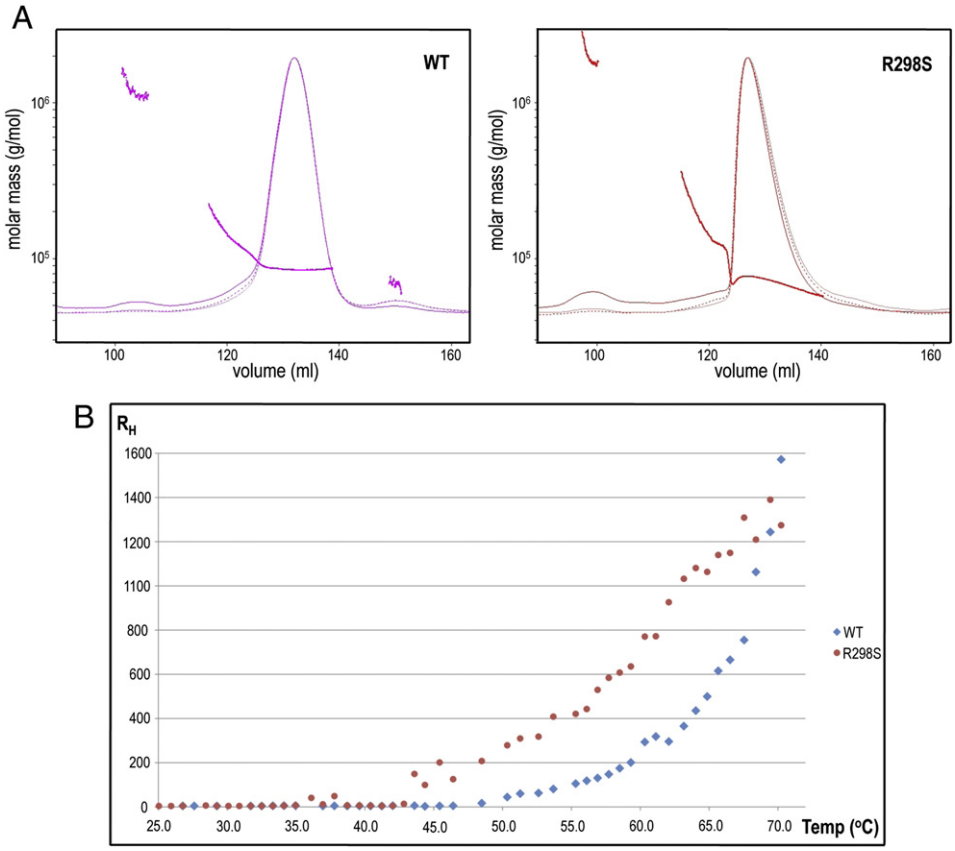

Fig. 3. Instability of Nt-R298S. **A.** Molecular-mass measurements are shown for wildtype Nt and Nt-R298S applied to a gel filtration column. MALS-SEC reveals a mixture of monomers and dimers across the peak for Nt-R298S, as reflected by the tail, and a weaker dimer or higher K_D than wildtype Nt. High-order clusters also are present in both traces: 1.2×10^6 Da ± 7.6% for wildtype and 2×10^6 Da ± 1.6% for the mutant. These clusters reappear upon filtration, also reflecting an equilibrium process. The increased molecular mass of the clusters in Nt-R298S may reflect the start of aggregates. **B.** Nt-R298S is less thermally stable than wildtype Nt. The onset temperature (T_m) for aggregation for Nt-298S is shifted ~3–5 °C compared to wildtype. The R_H for Nt-R298S also appears to take off nearly linearly. On the other hand, there is slower increase in R_H for wildtype until 60 °C, when the slope starts increasing significantly. Both linear or hyperbolic shapes of the curves suggest that the Nts aggregate rather than unfold at high temperatures, where unfolding is typically signified by a sigmodial-shaped curve. The consistently higher values of the linear curve also suggest that Nt-R298S is more prone to aggregation than wildtype.

vesicles. Fig 2A illustrates HCE cells expressing GFP-NBCe1-A localized at the plasma membrane shown by the green and red fluorescence overlap. The average intensity (n = 50) of the GFP-signal at the plasma membrane is 10,453 ± 7636 (16 bit pixel depth). In contrast, Fig 2B illustrates HCE cells expressing GFP-NBCe1-A-R298S localized at the plasma membrane and aggregated intracellularly in a string-like appearance of the GFP fluorescence near the membrane (See lower left panel). The average intensity (n = 50) of GFP-signal at the plasma membrane is 79% of wildtype, i.e., 8289 ± 5460, and 1 in 4 of HCE cells visibly exhibits the string-like aggregation.

Lastly, we tested to see if there is a difference in localization between polarized and non-polarized cells. Expression of GFP-NBCe1-A and GFP-NBCe1-A-R298S in polarized and non-polarized cells yielded similar results.

3.2. Instability of the Nt-298S dimer

In order to investigate the mechanism of the NBCe1-A-R298S aberration at the protein level, we purified and characterized the cytoplasmic, Nt domains of NBCe1-A and the NBCe1-A-R298S mutant. As shown in Fig 3A, immediately after purification, the M_W across the main peak measured by the MALS-SEC technique is 86 kDa ± 1.1% for the wildtype Nt and 73 kDa ± 2.4% for the Nt-R298S mutant at pH 7.3. The wildtype is all dimer in agreement with the theoretical molecular mass of 83.4 kDa and as indicated by the flat M_W trend. Because the dimer has been established to be in a reversible self-association in Gill (2012), and we now report in Fig 4C the K_D for the wild-type Nt monomer-dimer equilibrium to be 0.1 μM based on CG-MALS techniques, the elution concentration at this condition (24.0 μM at the apex and 0.3 μM at each edge) is much higher than the K_D for the monomer–monomer interaction. The Nt-R298S mutant in Fig 3A, however, demonstrates a concave M_W trend at this same condition. At the apex of the peak, where the eluting concentration is highest (22 μM), the dimer predominates. At the leading (0.9 μM) and trailing (0.3 μM) edges, where the concentrations are low, there is more monomer species. This variation of M_W across the peak signifies monomer–dimer equilibrium and indicates that the K_D for the mutant is much higher than wildtype, revealing a relatively weak Nt-R298S dimer. Over the course of hours to days at room temperature, the M_W of the Nt-R298S drops unlike wild type that remains a stable dimer even after a week. Mild concentration of the Nt-R298S results in visible precipitation, hindering further studies. This type of time- and concentration-dependent irreversible aggregation leading to precipitation of Nt-R298S purified at physiological pH has been observed in wild-type Nt but only when purified at alkaline pH greater than 8 [25]. Only a low concentration of protein remains in solution.

In Fig 3B, the instability and low solubility of the Nt-R298S mutant are further characterized by T_m studies that demonstrate an earlier onset of irreversible aggregation compared to wildtype Nt. Nt-R298S has an onset of ~43 °C compared to wildtype that has an onset of

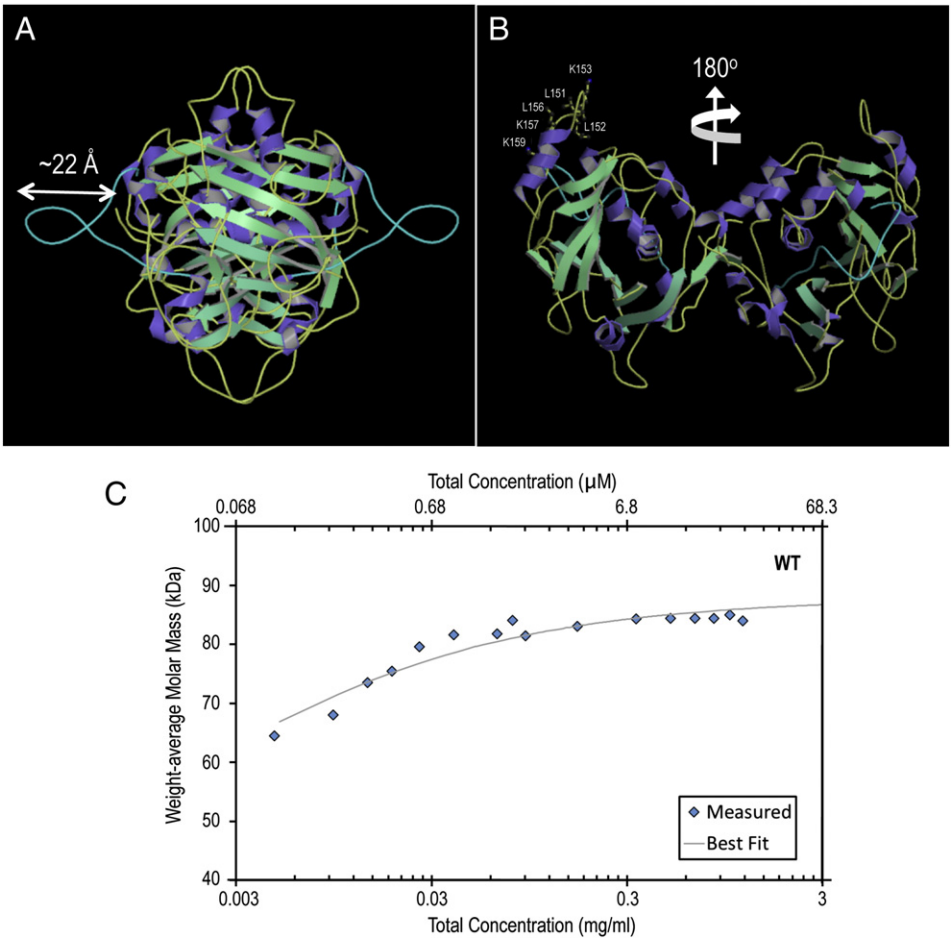

Fig. 4. Crystal model and monomer–dimer equilibrium measurement of Nt. **A.** Side-view of the Nt dimer, **B.** Front view of the Nt dimer. **C.** Monomer–dimer equilibrium study of the Nt. The crystal models are oriented so that the membrane is above and the cytoplasm is below. Helixes are colored purple, ß-strands are green, and loops are yellow or green. In **A**, the solvent extended loop of the Nt is highlighted in green and is the most notable structural difference between Nt of NBCe1 and Nt of AE1 [20]. In **B**, the dimer is held by two-interlocking arms from each subunit. In **C**, the Nt is revealed to actually be in equilibrium, by the drop off in molecular mass as a function of concentration. Three concentration gradients were performed, one beginning at ~3 mg/ml, at ~0.3 mg/ml, and another at ~0.03 mg/ml. These are independent experiments, and the data overlays and lines up within an error of 5%, and also are corroborated by the SEC-MALS experiments in Fig 2.

~48 °C. Interestingly, a hotspot occurs at 37 °C or body temperature, where the autocorrelation functions of both Nt-R298S and wild type reveal reversible large clusters that disappear before onset, suggesting that the Nts are more dynamic at this temperature. Finally, it is noteworthy that the rates of the increase of R_H are different, reflecting that Nt-R298S is less stable than wildtype.

3.3. Crystal structure of Nt and comparison to NtAE1

The Nt crystallized as a dimer in the asymmetric unit with total mass 83.4 kDa. Fig. 4A & B shows the structure oriented so that the TMD is above and the cytoplasm is below. Both monomers in the dimer are interlocked by swapping or exchanging arms. Electron density for residues 1 to 62, which encompasses the variable V1 region in the amino-acid sequence (residues 1–41) among SLC4 family members, is missing and suggests a high atomic-displacement factor for this segment or gate that would face the cytoplasm. The orientation in Fig 4A reveals that residues 185 to 207 form an accessible loop that extends 22 Å into solvent from the Nt surface. The loop corresponds to the variable V2 region in the amino-acid sequence. Each loop is stabilized by crystal contacts with neighboring dimers in the lattice [35]. The length of the loop is a defining character that distinguishes it from the crystal structure of family member NtAE1. The Nt loop is twice as long as the NtAE1. Except for this loop, superposition of the Nt with NtAE1 demonstrates that the overall structures are similar, having a RMSD of 1.9. The gap between each subunit is wider in the Nt, which was crystallized with a final pH of ~6.7 [35], than NtAE1, which was crystallized with a final pH ~4.9 [44] or 6.5 [45]. Fig 4B shows residues 142 to 158 form surface loops in each monomer that are on top of the structure and face the membrane. These loops are in an extended conformation compared to the crystal structures of NtAE1. The loop of Nt contains a mixture of hydrophobic side-chains from leucines (L151, L152, L156) and positively-charged lysines (K153, K157, K159) that are possibly involved in lipid interactions with the membrane, thereby stabilizing the Nt in the cytoplasm.

3.4. In-silico identification of putative Nt conduits

Using the higher resolution and complete crystal structure of NtAE1, the Nt core (missing the exterior V2 loop) was analyzed. Analysis of the Nt core reveals two components: (i) putative entrances (holes) into the Nt; and (ii) putative routes or conduits branch off from these entrances. First, a surface-representation of the Nt molecule's structure illustrates entrances into the Nt. Fig 5 shows the side and top view of the Nt dimer. The brown circle at the bottom is the foyer, which is visible only in the side view. Whereas the two yellow ovals in the top view mark the exit points. Note that only one yellow oval is visible in the side view. Indeed, the crystal structure of NtAE1 contains a few water molecules at the entrance sites. Second, the program CAVER illuminated two water paths within the Nt core, one of which is represented as the blue plume in Fig 5. One of the accessible conduits is traced through the interior of the Nt dimer as indicated by the dashed white path; this path through the interior of the dimer connects the foyer entrance to one of the conduit exits. A second path shown by the dashed magenta path connects the foyer entrance to the other conduit exit, which is not visible in the side view. The paths also coincide with a few water molecules that are identified in the NtAE1 crystal structure, giving support to a hypothesis that the conduits serves as routes for small molecules. The conduit opens to the TMD on one end and an apparent foyer entrance on the opposite end. Finally, the routes are in the proximity of R298 that is mutated to serine in patients. Here, the structure demonstrates the relative location of R298 as buried in the dimer interface. Thus, R298 is inaccessible to solvent unless of dimer disassociation into monomers, which occurs completely at pH 11.5 as previously reported [25].

3.4. Rescue of trafficking defect

The evaluate the possibility that NBCe1-A-R298S is temperature-sensitive based on our biophysical assessment, using Fig 3B as a guide, we set out to determine whether trafficking in HK-2 cells could be restored at lower temperature. Cells were transfected under the same conditions as Fig 1B except grown at 28 °C. In parallel, we repeated growth at 37 °C. At 28 °C, all cells ($n = 10$) transfected with GFP-NBCe1-A-R298S showed a large amount of GFP-signal successfully localized at the basolateral plasma membrane. Whereas at 37 °C, again only 10% of cells ($n = 10$) transfected with GFP-NBCe1-A-R298S at best showed a minor amount of GFP-signal at the membrane. Fig 6 demonstrates a HK-2 cell expressing the GFP-NBCe1-R298S defect rescued by the lower temperature.

4. Discussion

This report provides a new perspective on the controversy surrounding the effects of the naturally occurring R298S human mutation and reconciles the apparent conflicting studies. An R to S mutation could produce detrimental effects to monomer–dimer-high-order equilibrium (or colloidal system), favoring the formation of monomers that are prone to aggregate and eventually precipitate. In our cellular studies, the string-like aggregation is most striking and is not seen in HCE cells expressing GFP-NBCe1-A. Instead, there are smaller vesicle-like bodies, which are most likely routine cargo vesicles containing GFP-NBCe1-A. The string-like aggregates are probably not connected with the endocytic pathway because they do not appear to be strongly positive for WGA-AF633, which binds the plasma membrane and marks endocytic vesicles. It is possible that GFP-NBCe1-A-R298S is retained in the endoplasmic reticulum due to improper folding or glycosylation. Improper folding by glycosylation issues is unlikely, however. The point mutation would not affect the two known glycosylation sites that are on

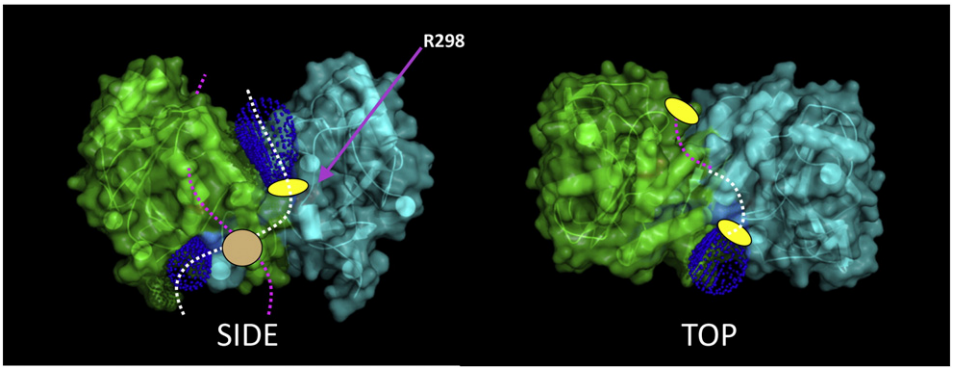

Fig. 5. Putative conduits in Nt core. The figure shows side & top views of the conduits (blue plumes) into the transmembrane domain. The conduits are lined by electrostatic residues (e.g. R298) that make up binding pockets. See text for a description of the transport pathways.

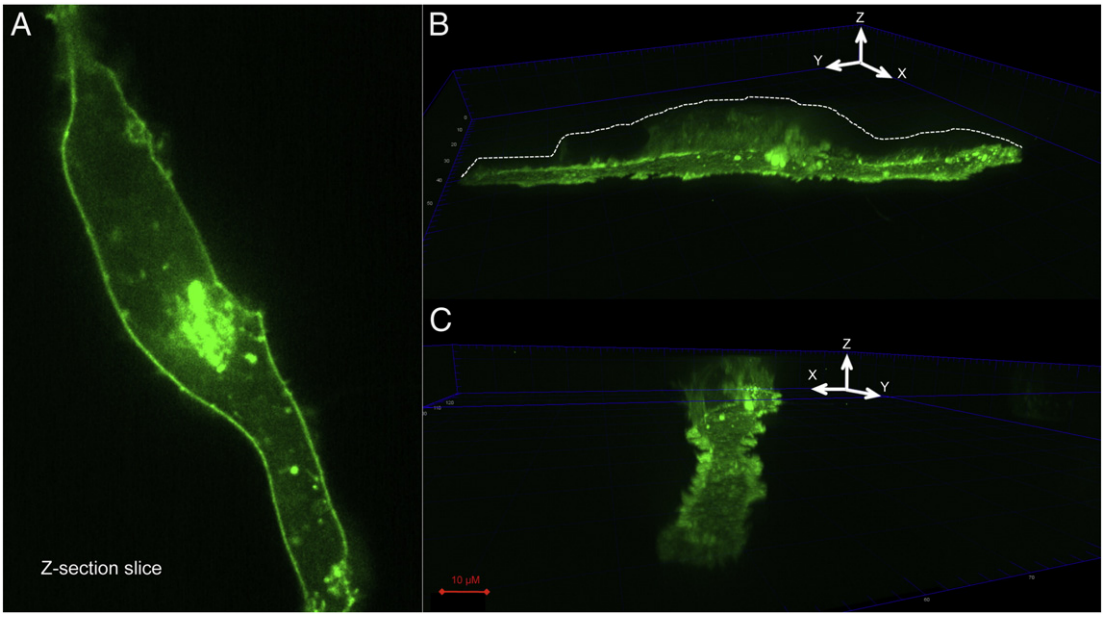

Fig. 6. Rescue of trafficking at low temperature. The figure shows fluorescent images of a polarized HK-2 cell grown at 28 °C and transfected with GFP-NBCe1-A-R298S, which demonstrates localization preference to the basolateral membrane. **A.** A cross-section through the Z-plane at the basolateral membrane is shown after excitation at 488 nm. GFP signal is observed in the membrane and inside the cell presumably within the nucleus and trafficking vesicle-like bodies. **B.** A three-dimensional view of the same cell in **A** is shown illustrating that the GFP signal in the membrane is located only on the basolateral side, which is attached to the glass coverslip that is gel-coated with poly-D-lysine. No GFP signal is observed on the apical side, whose surface is represented by the dotted lines. **C.** The same cell in **B** but rotated 90° along the Z-axis. The three-dimensional images were made with the Imaris software.

the extracellular loops of NBCe1. As observed, the fact that the mutant is largely expressed in HCE membranes demonstrates its ability to be targeted to the membrane. Importantly, we showed trafficking to the membrane by the GFP-mutant in HK-2 cells after growing them at a reduced temperature. The proper processing of the mutant is also supported by Igarashi et al. [7] and Horita et al. [8] whose studies in ECV304 cells showed that the mutant was targeted to the membrane. The efficacy of our recombinant expression plasmid is supported by Suzuki et al. [21] in MDCK cells and Parker at el. [42] in *Xenopus* oocytes who showed glycosylation by Western Blots and surface expression using the same expression construct as our studies. In Parker et al. three bands were visible by Western blots: (1) a ~150 kDa band close to the predicted molecular weight of unglycosylated monomeric GFP-NBCe1 (2) a diffuse ~170 kDa band that likely represents glycosylated monomer and (3) a ~300 kDa band that likely represents SDS stable dimers of GFP-NBCe1. Subcellular localization could be further explored using higher resolution imaging approaches, or double labeling with ER markers such as calnexin.

At first glance, the arginine at position 298 does not appear to be important for maintaining proper tertiary protein structure, and patients affected by this mutation have blood with acidic pH values (~7.1) that would favor dimer formation. This result, alone, suggests that the mutation results in a functional defect in substrate transport occurring inside the Nt. However, a mutation to serine at this site, where the hydroxyl group could compete for hydrogen bonding and thus destabilize the interface and affect the positions of nearby residues, might also have significant consequences on the stability of the dimer. Fig 7A illustrates a mechanism by which R298S might weaken the dimer configuration, while Fig 7B shows how this weakened dimer would result in aggregation and eventual precipitation. We propose a model whereby the R298 residue normally forms part of an electrostatic substrate pocket within the conduit and supports nearby residues that stabilize intermolecular β-strand interactions at the dimer interface. The hydroxyl group of the replaced serine residue randomly competes for H-bonding and disrupts the pocket. A weakened dimer interface, which is accelerated at higher expression levels, pushes the equilibrium to monomers, which non-specifically aggregate over time. Cell trafficking and plasma membrane incorporation depend on the remaining colloidal level. Our model ties together the observations reported in the literature.

Earlier cited contradictions regarding R298S may have arisen because the expression systems employed for investigating functional and trafficking mechanisms were not equivalent to native human proximal tubule or corneal cells in which NBCe1-A are expressed. Because each animal cell line behaves differently under particular stimuli [22], it can be difficult to draw relevant conclusions unless an appropriate model is used. Indeed, it is possible that native cells may contain multiple channel types or lipids that are absent in *Xenopus* oocytes and other cell types. Because *Xenopus* oocytes have been shown to utilize different cellular trafficking pathways than other cells, studies that use this model system may be at a disadvantage [46]. Even considering the equivalent mutation in AE1 to NBCe1-A-R298S, AE1-R283S, which was cited to traffick to the plasma membrane in HEK293 cells [45], HEK293 cells should not be used as an in vitro model for kidney cell function, being more closely related to immature neurons [47].

Regardless of cell type, the rate of Nt aggregation appears to be dependent on at least three criteria that may have not been consistent among other experiments described in the literature: concentration, pH, and temperature. When GST-tagged Nt-R298S was produced at a high concentration (~10 mg/ml), we observed that most of the purified Nt precipitated out of solution after release from glutathione beads. When a HIS-tagged mutant Nt was produced at a lower concentration (~1 mg/ml), the sample initially was soluble, and behaved similarly in character to wild type; however, this sample quickly transitioned into monomers and also slowly precipitated after a concentration step subsequent to purification.

Another factor that can influence Nt aggregation is pH. For example, we know that the buried dimer interface and the solvent-exposed V1 tail of wild-type Nt are pH sensitive. Keeping the wild-type Nt at pH less than 7.3 resulted in an impressively stable state. The observed instability of Nt-R298S at pH 7.3 mimicked the large monomeric population and aggregative states of wild-type Nt when exposed to pH values greater than 8 [25]. Complete dissociation of dimers occurs when the

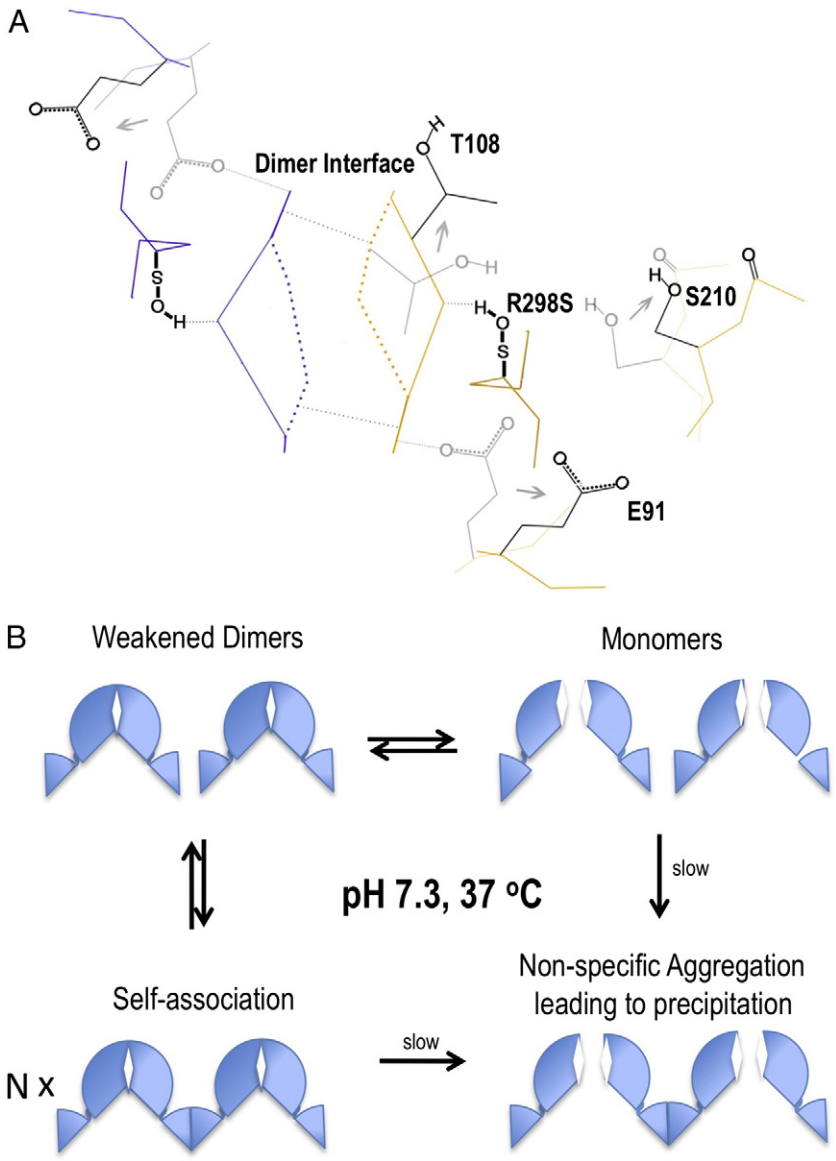

Fig. 7. Schematic mechanism of how R298S leads to abnormal aggregation. **A.** The figure shows the residues near the buried Nt-dimer interface, with each monomer colored by purple or gold. The monomers are related by a two-fold rotation, which is perpendicular to the page. The dimer is partially held together by hydrogen-bond interactions, which are shown by black dotted lines, from adjoining ß-strands, which are schematically drawn as dashed colored vertical lines. Each ß-strand within a monomer is supported by R298 through a hydrogen bond with T108. In addition, R298 coordinates with nearby residues in a hydrogen-bond network consisting of the carboxyl group of E91, the hydroxyl group of S210 and a neighboring carboxyl-group on the backbone, as judged by atomic distances less than 3.5 Å. These residues may comprise a substrate pocket. A R298S mutation buried within the Nt is shown to result in the collapse of ß-strands (solid vertical line) and a proposed destruction of a substrate-binding pocket within the Nt core. **B.** The weakened dimer in **A** is schematically drawn to illustrate how the shifted residues at the interface may affect the Nt monomer-dimer-high-order equilibrium, leading to free-monomers that aggregate and fall out of solution. This illustration is also based on our work in Gill (2012).

Nt is exposed to pH 11.5 [25]. In other prior studies, an R298C mutation in NBCe1-A that had been solubilized from the cell membrane at pH 11.5 significantly increased labeling with the cysteine-specific reagent biotin maleimide [48]. Taking our model into account, this change in labeling efficiency suggests that NBCe1-A-R298C was in a monomeric state, and thus more accessible to labeling reagent. We believe that in the aforementioned cases, the alkaline pH resulted in the loss of stabilizing hydrogen bonds.

Although understudied in this field, temperature change can have an effect on Nt self-association and aggregation. Besides the aforementioned differences in cell types, another possible explanation for the differences in trafficking pathways between *Xenopus* oocytes and HK-2 cells is variation in cell-growth temperature. *Xenopus* oocytes are typically grown at 28 °C, while HK-2 cells are grown at 37 °C. Additionally, NBCe1-A activity is sensitive to changes in temperature. Indeed, protein folding, misfolding, and clustering are generally all highly temperature-sensitive processes, and Fig 3B shows that Nt-R298S is in a more dynamic state at 37 °C compared to 28 °C. An example of how temperature dependence can affect the outcome of experiments can be seen in studies involving the Δ508 deletion mutant of cystic fibrosis transmembrane conductance regulator (CFTR), which has been linked to cystic fibrosis [49]. Studies showing that this mutant formed a functional chloride channel in *Xenopus* oocytes, but not in cultured cells, illustrated that the mutant's effect on trafficking is temperature dependent [50,51]. Taking these observations into account, we would expect a largely functional NBCe1-A-R298S dimer, with diminished activity due to missing positive charges that weaken the binding pocket within the Nt of NBCe1, but only when this protein is properly integrated into the plasma membrane of *Xenopus* oocytes.

Besides temperature, local pH and protein concentration that could be different among cell lines, there are likely a number of other factors at play that could account for the inconsistency of GFP-NBCe1-R298S levels in the membrane observed between Fig 1B and Fig 2B. Each cell line could traffick and glycosylate proteins differently. Even heat-sensitive chaperones could vary among cell lines. Heat-shock proteins, like HSP25, HSP70, HSP90, or alpha-crystallin that has chaperone-like activity, could vary between kidney and eye cells [52–56].

Transport conduits that are hypothesized to be within the Nt, based on in silico analysis, have been illustrated for the first time in the Nt domain of family member AE1 (NtAE1). These conduits begin at a highly disordered flexible segment of the solvent facing dimer interface (N terminus), pass in close proximity to R298 (or its equivalent R283 in NtAE1), and end at the membrane-associated interface (C terminus). Fig 5 highlights a hypothesized pathway that, based on our space calculations, comes into close proximity to R298, a residue that is known to affect the rate of transport. In our modeled pathway (Fig 5), the pathway highlighted by the blue plum was calculated to lead to the side of the entrance, rather than between the green and blue ends at the bottom entrance. We believe that this entrance between the interlocking arms is closed, because the Nt is in a taut state due to acidic pH conditions, thus blocking the pathway and forcing it to come out at the side. At a more neutral pH, the Nt is in an open state and the blue plum will naturally come out exactly between the two interlocking arms. We suspect the rest of the transport pathway involving R298 will be the same for both NtAE1 and the Nt because superposition analysis of the two protein backbones showed they are similar in structure. Our results here are consistent with biophysical studies by Shnitsar et al., who also acknowledged the possibility of substrate access tunnels in NtAE1, and in agreement with our studies here provided evidence that the equivalent mutation R283S destabilizes the structure [45].

Lastly, our assertion of NBCe1-A in monomer–dimer equilibrium applies to both the cytoplasmic Nt and the transmembrane domain (TMD) even as individual components. The evolutionary pattern of the SLC4 N-terminal domain is very similar to that of the full-length SLC4 proteins, implying that each Nt and TMD coevolved as illustrated by the dendrogram in Gill & Boron [31]. Therefore, the Nt and TMD are likely functionally integrated, though the cytoplasmic Nt seems to be the underlying driving force (motor) behind forming larger self-associations or patches in membranes. For the Nt domain of NBCe1, we demonstrated the equilibrium in Fig. 4C, where we extract for the first time a disassociation constant value. For the TMD of NBCe1, our model is based on parallel work on family member AE1, which has an amino-acid sequence percent identity above 30% that confirms structural identity as partially illustrated here by the high overlap in crystal structures of their core regions. While we already know that full-length AE1 is in monomer–dimer equilibrium [26], though the dissociation constant has yet to be measured, the question arises whether the TMD by itself could be in equilibrium. Fig. 4 of Rettig et al. [26] shows the TMD domain of AE1 (or AE1 with the Nt enzymatically removed) run over a size-exclusion column. Like the Nt domain of AE1, the TMD domain of AE1 clearly shows two species (i.e. monomer and dimer) whose relative populations are pH dependent. This chromatogram looks identical to our previously published studies on the Nt of NBCe1 in Gill [25]. We also can see that at higher pHs, the TMD domain of AE1 demonstrates “abnormal aggregation” as indicated by the broader peaks and the larger peak at 5 ml elution volume, which is very similar to our published observations of the Nt of NBCe1 in Gill [25]. The low expression levels in tissues of most SLC4s other than AE1 expressed in RBCs do not permit detailed biophysical studies on all TMDs in the family. We will point out, however, other known autosomal-recessive mutations that occur in the TMD regions are likely to be temperature-sensitive in nature as well.

5. Conclusions

Taken together with our previous [25,35] and concurrent work [57], the Nt plays a multifunctional role in dimerization, membrane patch formation, substrate transport and trafficking to the membrane in human HK-2 and HCE cells. It is therefore apparent that a major aberration in Nt would promote the observed losses of the entire co-transporter capabilities in both trafficking and cotransport. The underlying aberration caused by R298S appears to be a temperature-sensitive one that breaks the monomer-dimer equilibrium, exposing charged surface patches on isolated monomers that aid in aggregation and eventual precipitation. Understanding the role of conduits could have implications in other NCBTs and in a wide range of channels and transporters. Protein concentration or cellular expression level, pH, and temperature are likely the effectors in patients with the R298S mutation and behind the apparent variable behavior observed in experiments among animal-model cell types. Our studies suggest lower temperatures, even by only a couple of degrees lower than body temperature, put less pressure on the fragile dimer likely by decreasing local cellular dynamics and/or protein concentration. Reminiscent to the poikilotherms whose body temperature is that of its surroundings, it is likely that those tissues in patients that are directly exposed to the environment are the ones less affected by the defect, while tissues that are better maintained at human-body temperature are more affected.

Acknowledgments

We thank Drs. Mary Lou King and Timothy McCaffrey for their discussion, Drs. Sophia Kenrick and Bob Collins for their help with the CG-MALS, Drs. Diego Gabriel Ogando, Shimin Li, Ali Ramezani, and Ms. Tara Kesteloot for their help with cell lines. Award Number K01DK082646 (Dr. H.S. Gill) from the National Institute of Diabetes and Digestive and Kidney Diseases (NIDDK) of the National Institutes of Health (NIH) supported this project. Dr. Anastas Popratiloff was supported by grant number P30HD040677 from the Intellectual and Developmental Disabilities Research Center (IDDRC) at Children's National Medical Center (CNMC).

Appendix A. Supplementary data

Support Information includes a table of Data and Model Crystal Statistics with an example 2Fo-Fc omit map, and additional 3-D images demonstrating HCE and HK-2 cell polarization. Supplementary data to this article can be found online at http://dx.doi.org/10.1016/j.bbagen.2015.02.014.

References

[1] T. Igarashi, T. Sekine, J. Inatomi, G. Seki, Unraveling the molecular pathogenesis of isolated proximal renal tubular acidosis, J. Am. Soc. Nephrol. 13 (2002) 2171–2177.
[2] M.F. Romero, C.M. Fulton, W.F. Boron, The SLC4 family of HCO(3)(−) transporters, Pflugers Arch. 447 (2004) 495–509.
[3] M.D. Parker, W.F. Boron, The divergence, actions, roles, and relatives of sodium-coupled bicarbonate transporters, Physiol. Rev. 93 (2013) 803–959.
[4] I. Kurtz, NBCe1 as a model carrier for understanding the structure–function properties of Na-coupled SLC4 transporters in health and disease, Pflugers Arch. 466 (2014) 1501–1516.
[5] T. Igarashi, T. Sekine, H. Watanabe, Molecular basis of proximal renal tubular acidosis, J. Nephrol. 15 (Suppl. 5) (2002) S135–S141.
[6] S.K. Haque, G. Ariceta, D. Batlle, Proximal renal tubular acidosis: a not so rare disorder of multiple etiologies, Nephrol. Dial. Transplant. 27 (2012) 4273–4287.
[7] T. Igarashi, J. Inatomi, T. Sekine, S.H. Cha, Y. Kanai, M. Kunimi, K. Tsukamoto, H. Satoh, M. Shimadzu, F. Tozawa, T. Mori, M. Shiobara, G. Seki, H. Endou, Mutations in SLC4A4 cause permanent isolated proximal renal tubular acidosis with ocular abnormalities, Nat. Genet. 23 (1999) 264–266.
[8] S. Horita, H. Yamada, J. Inatomi, N. Moriyama, T. Sekine, T. Igarashi, Y. Endo, M. Dasouki, M. Ekim, L. Al Gazali, M. Shimadzu, G. Seki, T. Fujita, Functional analysis of NBC1 mutants associated with proximal renal tubular acidosis and ocular abnormalities, J. Am. Soc. Nephrol. 16 (2005) 2270–2278.

[9] R.S. Satoskar, S.D. Bandarker, N.N. Rege, Pharmacology and Pharmatherapeutics, 21st ed Popoular Prakashan Private Limited, Mumbai India, 2009.
[10] M. Suzuki, G. Seki, H. Yamada, S. Horita, T. Fujita, Functional roles of electrogenic sodium bicarbonate cotransporter NBCe1 in ocular tissues, Open Ophthalmol. J. 6 (2012) 36–41.
[11] F.Y. Demirci, M.H. Chang, T.S. Mah, M.F. Romero, M.B. Gorin, Proximal renal tubular acidosis and ocular pathology: a novel missense mutation in the gene (SLC4A4) for sodium bicarbonate cotransporter protein (NBCe1), Mol. Vis. 12 (2006) 324–330.
[12] M. Chesler, Regulation and modulation of pH in the brain, Physiol. Rev. 83 (2003) 1183–1221.
[13] M. Suzuki, W. Van Paesschen, I. Stalmans, S. Horita, H. Yamada, B.A. Bergmans, E. Legius, F. Riant, P. De Jonghe, Y. Li, T. Sekine, T. Igarashi, I. Fujimoto, K. Mikoshiba, M. Shimadzu, M. Shiohara, N. Braverman, L. Al-Gazali, T. Fujita, G. Seki, Defective membrane expression of the Na(+)–HCO(3)(−) cotransporter NBCe1 is associated with familial migraine, Proc. Natl. Acad. Sci. U. S. A. 107 (2010) 15963–15968.
[14] H.H. Damkier, S. Nielsen, J. Praetorius, Molecular expression of SLC4 derived Na+ dependent anion transporters in selected human tissues, Am. J. Physiol. Regul. Integr. Comp. Physiol. 293 (2007) R2136–R2146.
[15] G. Deda, M. Ekim, A. Guven, U. Karagol, N. Tumer, Hypopotassemic paralysis: a rare presentation of proximal renal tubular acidosis, J. Child Neurol. 16 (2001) 770–771.
[16] D. Dinour, M.H. Chang, J. Satoh, B.L. Smith, N. Angle, A. Knecht, I. Serban, E.J. Holtzman, M.F. Romero, A novel missense mutation in the sodium bicarbonate cotransporter (NBCe1/SLC4A4) causes proximal tubular acidosis and glaucoma through ion transport defects, J. Biol. Chem. 279 (2004) 52238–52246.
[17] R.S. Lacruz, A. Nanci, S.N. White, X. Wen, H. Wang, S.F. Zalzal, V.Q. Luong, V.L. Schuetter, P.S. Conti, I. Kurtz, M.L. Paine, The sodium bicarbonate cotransporter (NBCe1) is essential for normal development of mouse dentition, J. Biol. Chem. 285 (2010) 24432–24438.
[18] J. Brown, S.J. Reading, S. Jones, C.J. Fitchett, J. Howl, A. Martin, C.L. Longland, F. Michelangeli, Y.E. Dubrova, C.A. Brown, Critical evaluation of ECV304 as a human endothelial cell model defined by genetic analysis and functional responses: a comparison with the human bladder cancer derived epithelial cell line T24/83, Lab. Invest. 80 (2000) 37–45.
[19] M.H. Chang, J. DiPiero, F.D. Sonnichsen, M.F. Romero, Entry to “HCO3 tunnel” revealed by SLC4A4 human mutation and structural model, J. Biol. Chem. 283 (2008) 18402–18410.
[20] D. Zhang, A. Kiyatkin, J.T. Bolin, P.S. Low, Crystallographic structure and functional interpretation of the cytoplasmic domain of erythrocyte membrane band 3, Blood 96 (2000) 2925–2933.
[21] M. Suzuki, M.H. Vaisbich, H. Yamada, S. Horita, Y. Li, T. Sekine, N. Moriyama, T. Igarashi, Y. Endo, T.P. Cardoso, L.C. de Sa, V.H. Koch, G. Seki, T. Fujita, Functional analysis of a novel missense NBC1 mutation and of other mutations causing proximal renal tubular acidosis, Pflugers Arch. 455 (2008) 583–593.
[22] R.A. Grant, T. Halliday, E. Chadwick, Amphibians' response to the lunar synodic cycle—a review of current knowledge, recommendations, and implications for conservation, Behav. Ecol. 24 (2012) 53–62.
[23] V.Y. Lugovtsev, D. Melnyk, J.P. Weir, Heterogeneity of the MDCK cell line and its applicability for influenza virus research, PLoS One 8 (2013) e75014.
[24] M.K. Joubert, Q. Luo, Y. Nashed-Samuel, J. Wypych, L.O. Narhi, Classification and characterization of therapeutic antibody aggregates, J. Biol. Chem. 286 (2011) 25118–25133.
[25] H.S. Gill, pH-Sensitive self-associations of the N-terminal domain of NBCe1-A suggest a compact conformation under acidic intracellular conditions, Protein Pept. Lett. 19 (2012) 1054–1063.
[26] M.P. Rettig, C.J. Orendorff, E. Campanella, P.S. Low, Effect of pH on the self-association of erythrocyte band 3 in situ, Biochim. Biophys. Acta 1515 (2001) 72–81.
[27] H.M. Van Dort, R. Moriyama, P.S. Low, Effect of band 3 subunit equilibrium on the kinetics and affinity of ankyrin binding to erythrocyte membrane vesicles, J. Biol. Chem. 273 (1998) 14819–14826.
[28] M.J. Ryan, G. Johnson, J. Kirk, S.M. Fuerstenberg, R.A. Zager, B. Torok-Storb, HK-2: an immortalized proximal tubule epithelial cell line from normal adult human kidney, Kidney Int. 45 (1994) 48–57.
[29] T. Schmedt, Y. Chen, T.T. Nguyen, S. Li, J.A. Bonanno, U.V. Jurkunas, Telomerase immortalization of human corneal endothelial cells yields functional hexagonal monolayers, PLoS One 7 (2012) e51427.
[30] Q. Wang, Y. Lu, M. Yuan, I.M. Darling, E.A. Repasky, M.E. Morris, Characterization of monocarboxylate transport in human kidney HK-2 cells, Mol. Pharm. 3 (2006) 675–685.
[31] H.S. Gill, W.F. Boron, Expression and purification of the cytoplasmic N-terminal domain of the Na/HCO3 cotransporter NBCe1-A: structural insights from a generalized approach, Protein Expr. Purif. 49 (2006) 228–234.
[32] D. Some, Light-scattering-based analysis of biomolecular interactions, Biophys. Rev. 5 (2013) 147–158.
[33] A.K. Attri, A.P. Minton, Composition gradient static light scattering: a new technique for rapid detection and quantitative characterization of reversible macromolecular hetero-associations in solution, Anal. Biochem. 346 (2005) 132–138.
[34] A.P. Minton, Static light scattering from concentrated protein solutions I: general theory for protein mixtures and application to self-associating proteins, Biophys. J. 93 (2007) 1321–1328.
[35] H.S. Gill, W.F. Boron, Preliminary X-ray diffraction analysis of the cytoplasmic N-terminal domain of the Na/HCO 3 cotransporter NBCe1-A, Acta Crystallogr. F Struct. Biol. Cryst. Commun. 62 (2006) 534–537.
[36] B.W. Matthews, Solvent content of protein crystals, J. Mol. Biol. 33 (1968) 491–497.
[37] K.A. Kantardjieff, B. Rupp, Matthews coefficient probabilities: improved estimates for unit cell contents of proteins DNA, and protein–nucleic acid complex crystals, Protein Sci. 12 (2003) 1865–1871.
[38] A.J. McCoy, R.W. Grosse-Kunstleve, L.C. Storoni, R.J. Read, Likelihood-enhanced fast translation functions, Acta Crystallogr. D Biol. Crystallogr. 61 (2005) 458–464.
[39] T.K. Jones, M, Model-building and refinement practice, Meth. Enzymol. 277 (1999) 173.
[40] G.J. Kleywegt, T.A. Jones, Software for handling macromolecular envelopes, Acta Crystallogr. D Biol. Crystallogr. 55 (1999) 941–944.
[41] P. Emsley, K. Cowtan, Coot: model-building tools for molecular graphics, Acta Crystallogr. D Biol. Crystallogr. 60 (2004) 2126–2132.
[42] M.D. Parker, X. Qin, R.C. Williamson, A.M. Toye, W.F. Boron, HCO(3)(−)-independent conductance with a mutant Na(+)/HCO(3)(−) cotransporter (SLC4A4) in a case of proximal renal tubular acidosis with hypokalaemic paralysis, J. Physiol. 590 (2012) 2009–2034.
[43] H.C. Li, P. Szigligeti, R.T. Worrell, J.B. Matthews, L. Conforti, M. Soleimani, Missense mutations in Na +:HCO 3− cotransporter NBC1 show abnormal trafficking in polarized kidney cells: a basis of proximal renal tubular acidosis, Am. J. Physiol. Ren. Physiol. 289 (2005) F61–F71.
[44] A.B. Kiyatkin, P. Natarajan, S. Munshi, W. Minor, J.E. Johnson, P.S. Low, Crystallization and preliminary X-ray analysis of the cytoplasmic domain of human erythrocyte band 3, Proteins 22 (1995) 293–297.
[45] V. Shnitsar, J. Li, X. Li, C. Calmettes, A. Basu, J.R. Casey, T.F. Moraes, R.A. Reithmeier, A substrate access tunnel in the cytosolic domain is not an essential feature of the solute carrier 4 (SLC4) family of bicarbonate transporters, J. Biol. Chem. 288 (2013) 33848–33860.
[46] A.L. Goldin, Expression of ion channels in *Xenopus* oocytes, in: J.C.D. Trezise (Ed.), Expression and Analysis of Recombinant Ion Channels, WILEY-VCH Verlag GmbH & Co. KGaA, Weinheim, 2006.
[47] G. Shaw, S. Morse, M. Ararat, F.L. Graham, Preferential transformation of human neuronal cells by human adenoviruses and the origin of HEK 293 cells, FASEB J. 16 (2002) 869–871.
[48] Q. Zhu, L. Kao, R. Azimov, D. Newman, W. Liu, A. Pushkin, N. Abuladze, I. Kurtz, Topological location and structural importance of the NBCe1-A residues mutated in proximal renal tubular acidosis, J. Biol. Chem. 285 (2010) 13416–13426.
[49] D.C. Gadsby, P. Vergani, L. Csanady, The ABC protein turned chloride channel whose failure causes cystic fibrosis, Nature 440 (2006) 477–483.
[50] J. Rennolds, P.N. Boyaka, S.L. Bellis, E. Cormet-Boyaka, Low temperature induces the delivery of mature and immature CFTR to the plasma membrane, Biochem. Biophys. Res. Commun. 366 (2008) 1025–1029.
[51] Y.J. Qadri, E. Cormet-Boyaka, A.K. Rooj, W. Lee, V. Parpura, C.M. Fuller, B.K. Berdiev, Low temperature and chemical rescue affect molecular proximity of DeltaF508-cystic fibrosis transmembrane conductance regulator (CFTR) and epithelial sodium channel (ENaC), J. Biol. Chem. 287 (2012) 16781–16790.
[52] K. Musial, D. Zwolinska, Heat shock proteins in chronic kidney disease, Pediatr. Nephrol. 26 (2011) 1031–1037.
[53] K. Morita, H. Wakui, A. Komatsuda, H. Ohtani, A.B. Miura, H. Itoh, Y. Tashima, Induction of heat-shock proteins HSP73 and HSP90 in rat kidneys after ischemia, Ren. Fail. 17 (1995) 405–419.
[54] U. Ramp, C. Mahotka, S. Heikaus, T. Shibata, M.O. Grimm, R. Willers, H.E. Gabbert, Expression of heat shock protein 70 in renal cell carcinoma and its relation to tumor progression and prognosis, Histol. Histopathol. 22 (2007) 1099–1107.
[55] D.R. Ciocca, S.K. Calderwood, Heat shock proteins in cancer: diagnostic, prognostic, predictive, and treatment implications, Cell Stress Chaperones 10 (2005) 86–103.
[56] J. Horwitz, Alpha-crystallin, Exp. Eye Res. 76 (2003) 145–153.
[57] H.S. Gill, C.N. Watkins, A. Popratiloff, Multifunctional role of the N-terminal variable (V1) domain of the sodium-bicarbonate cotransporter NBCe1-A: patch formation trafficking & gating, J. Am. Soc. Nephrol. 24 (2013) 75A.